Solid Freeform Fabrication 2023: Proceedings of the 34th Annual International
Solid Freeform Fabrication Symposium – An Additive Manufacturing Conference
Reviewed Paper

EXPLORING IN718 ALLOY PRODUCTION WITH BI-DIRECTIONAL RASTER AND STOCHASTIC SPOT MELTING TECHNIQUES USING AN OPEN-SOURCE ELECTRO 1 %($0 MELTING SYSTEM

S.T. Nabil*†, C. Banuelos*†, B. Ramirez*†, A. Cruz*†, K.I. Watanabe*†, E. Arrieta *†,
R.B Wicker*† and F. Medina*†

*Department of Aerospace and Mechanical Engineering, University of Texas at El Paso, El Paso, Texas, 79968
†W.M Keck Center for 3D Innovation, University of Texas as El Paso, Texas, 79968

Keywords: Electron Beam Powder-Bed Fusion (E-PBF), Scanning Strategies, Superalloys, Inconel 718

Abstract

This study compares the fabrication of IN718 alloy using bi-directional raster and stochastic spot melting techniques with the open-source FreemeltOne Electron Beam Melting (EBM) system. The research aimed to produce dense parts using both scanning strategies, employing custom Python code for raster melt beam path generation and PixelMelt software for stochastic spot melting path generation. After optimizing process parameters, 10mm height builds for each scanning strategy were fabricated, and their microstructure, hardness, and density were analyzed using optical microscopy and SEM, Vickers microhardness scale, and a pycnometer. The findings reveal valuable insights into the effects of scanning strategies on the microstructure, hardness, and density of IN718 alloy components, advancing additive manufacturing knowledge.

Nomenclature

PBF – Powder Bed Fusion
EB-PBF – Electron Beam Powder Bed Fusion
IN718 – Inconel 718 (Nickel Based Alloy)
µm – Microns
µs - Microseconds
mm - Millimeters
E_a – Energy Per Area (J/mm^2)
°C – Degree Celsius
E_{as} - Energy Per Area Spot(J/mm^2)

1 Introduction

The aerospace and defense sectors are in constant pursuit of materials that exhibit excellent strength and resistance to deformation at high temperatures. Nickel-based superalloys, particularly Inconel 718 (IN718), have gained considerable attention due to their superior strength, versatility, and resistance to corrosion even at elevated temperatures up to 650°C [1]. Additionally, these alloys display commendable weldability and formability. This alloy is mostly composed of nickel, iron, chromium, niobium, molybdenum, titanium, cobalt, and small amounts of aluminum and iron. The exact composition ranges from 50-55% nickel, 17-21% chromium, 4.8-5.5% niobium, 2.8-3% molybdenum, 0.65-1.15% titanium, 1% cobalt, with the remainder being iron and aluminum [2,3]. Its phase composition primarily includes a γ matrix, enriched with precipitates of γ', γ'', δ, and certain carbides [4,5].

IN718 alloys are widely in focus due the the capability of them being produced additively through metal Additive Manufacturing. The most common and widely used metal AM technologies are – Powder Bed Fusion (PBF), Directed Energy Deposition (DED), and BinderJetting (BJT). Among them, PBF has already wide recognition for producing IN718 parts. EB-PBF is one type of PBF machine that uses an electron beam in a vacuum chamber and melt the materials layer by layer. In recent years, a sum amount of research has been conducted using EB-PBF to produce IN718 parts using commercial EB-PBF machines exploring novel scanning strategies to control the microstructure [6,7,8,9].

This research work will evaluate the fabrication of IN-718 alloy using an open source EB-PBF machine called FreemeltOne (Freemelt AB, Sweden) using two different scanning strategies : Bi-directional raster and stochastic spot melting. The goal of this study was to identify differences in terms of microstructure, hardness and density for IN718 in raster scan and spot melt scanning strategy.

2 Methodology

Feedstock Characteristics

The powder utilized for this research was plasma-atomized, spherical IN718 powder obtained from vendor AP&C. It exhibited a particle size distribution ranging from 45 to 106µm, with respective D10, D50, and D90 values measured at 52µm, 73µm, and 105µm. The powder's flowability was measured using a hall flowmeter following the ASTM B213-20 standard and was found to be 11s/50g, indicating satisfactory flowability for the PBF application.

EB-PBF System

The machine used for part fabrication was FreemeltOne EB-PBF machine (Freemelt AB, Sweden). It uses CO_2 laser to heat up the cathode (LaB_6) in vacuum and uses electron beam to melt metal powders layer by layer. The machine operates at 60kV in a vacuum with base pressure ranging from from10^{-6} hPa (mbar) to 10^{-7} hPa (mbar). The maximum beam power for this machine is 6kW. The print process for the FreemeltOne is divided into four stages, namely startheat, preheat, melt and postheat, which are executed sequentially in each cycle during printing.

Process Parameters

Stainless steel build substrate was used as build plate. At the beginning of the building, the plate was heated to 1050°C using a custom-coded beam pattern. After that, as powders were spread of 0.75 µm layer thickness to the build plate, a sequence of preheat patterns was employed to preheat the powder to minimize smoke events. Next, melt was done and the process repeated itself.

For the Melt process, two different scanning strategies: Bi-directional Vector Raster (Figure 2.1a) and Stochastic Spot Melt (Figure 2.1b) were implemented.

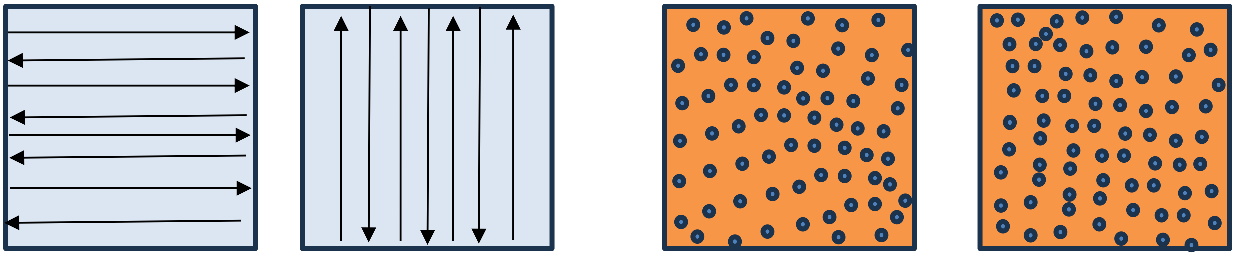

(a) Bi-directional Raster Scan N and n+1 layers

(b) Stochastic Spot melt n and n+1 layers

Figure 2.1 Schematic diagram for Bi-directional Raster and Spot Melt Strategy

For the raster scan – python script was written to generate open beam path file (.obp) which dictates the beam path. For the Spot melt, cloud-based PixelMelt software (Freemelt, AB, Sweden) was used to prepare the build obp file for the melt. In both cases, a build of 10mm height was done. For raster, the shape of the build was square of 15x15mm and for spot melt it was circular geometry of diameter 15mm.

For the raster and the spotmelt parameters for melt is explained by Table 2.1 below:

Table 2.1: Process Parameters

Scanning Strategy	Parameter Type	Values
Raster Melt	Power	300W
	Speed	800mm/sec
	Line Offset	0.1mm
	E_a (J/mm^2)	3.75J/mm^2
Stochastic Spot Melt	Power	360W
	Mesh Size	0.1mm
	Beam Dwell	0.250 milliseconds
	E_{as} (J/mm^2)	9J/mm^2

Microstructure Characterization

To analyze the microstructure of the builds, sectioned pieces were cut along the build directions and then hot-mounted using an ATM Opal 460 (Haan, Germany). These samples were further prepared by mounting and polishing them with the help of an ATM SAPHIR 530 (ATM GmbH, Germany) semi-automatic system. To reveal the microstructure, Kralling's No. 2 etchant was used. The etched samples were then observed using a Keyence VHX 7000 (Keyence Corp., Japan) Series digital microscope. To investigate deeper into the details of grain boundaries, Scanning Electron Microscope (SEM) images were taken using a Jeol SEM machine, with the imaging plane oriented in the build direction.

Density and Hardness

The density of the built samples was measured using the Accupyc II 1340 (Micromeritics Instruments, USA) series pycnometer, which utilizes helium as its operating gas. For the hardness measurements, the CHD Master microhardness tester (QATM, Germany) with the Vickers scale (HV1) was employed.

3 Result and Discussion

Microstructure Characterization

The as-polished microstructures, oriented along the build direction, for both the raster and stochastic spot melt techniques, are illustrated in Figure 3.1. Raster melt build had lower porosity than stochastic spot melt-observed in as-polished microstructure.

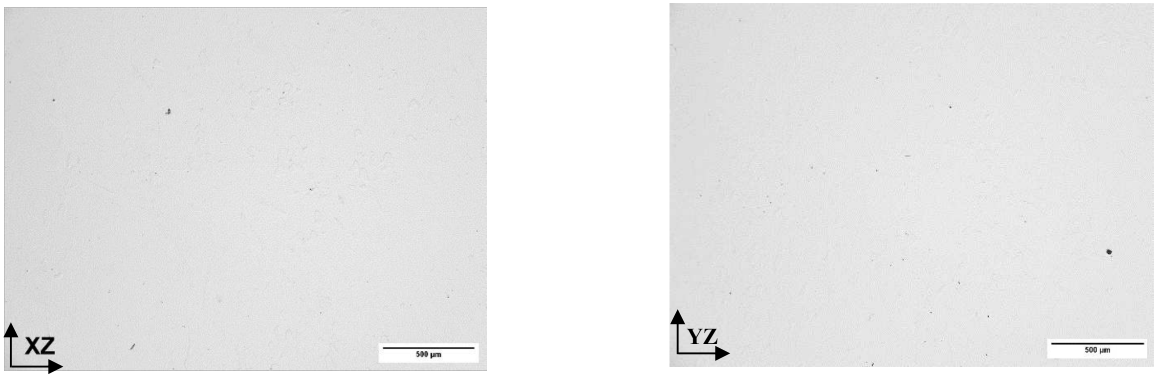

a) Raster Melt (contrast and sharpness enhanced)

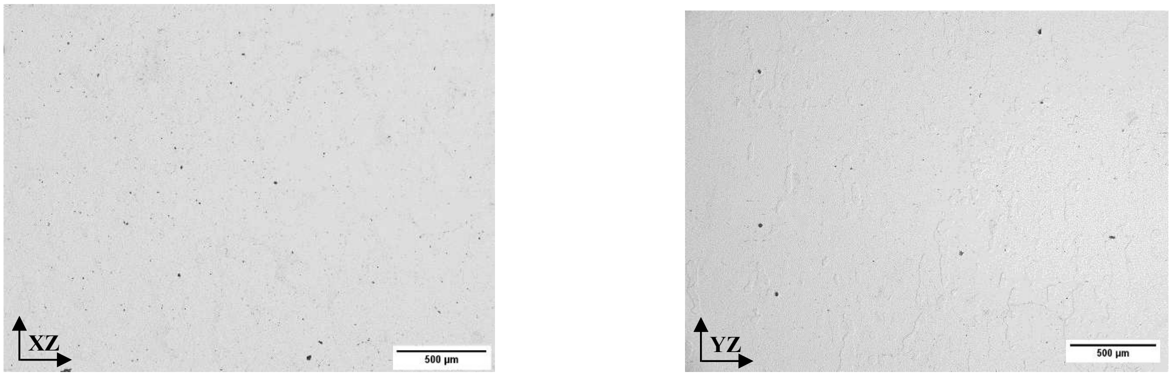

b) Stochastic Spot Melt (contrast and sharpness enhanced)

Figure 3.1 (a) As-Polished (Raster) ; (b) As-Polished (Stochastic Spot Melt)

During the stochastic spot melt process, higher energy was required to obtain a dense build which might contributed in resulted porosity. It was observed that – if the same E_{as} was maintained, by altering high power, lower spot dwell time, or low power and higher spot dwell time – two different cases occurred.

For case I, lower power higher spot dwell, a concentrated porosity was at the center of the specimen in the build direction (Figure 3.2a). For case II, high power and lower spot dwell time, small porous regions were observed all over the specimen (Figure 3.2b). Therefore, the later process parameter was chosen as the optimized condition for the stochastic spot melt method as displayed in Table 2.1.

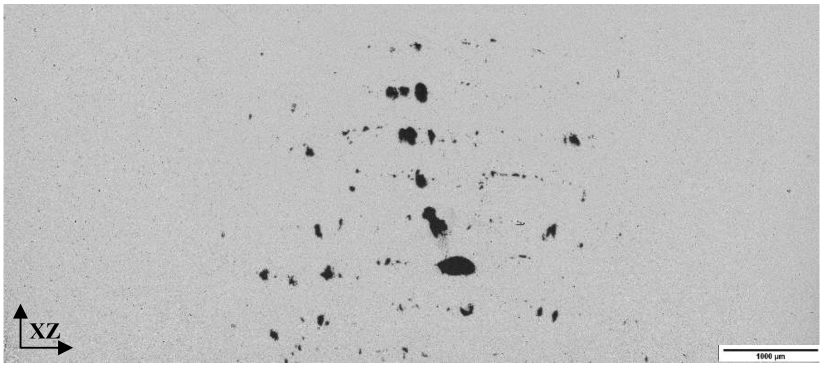

a) Case I: High power, low dwell time, E_{as} Constant (contrast and sharpness enhanced)

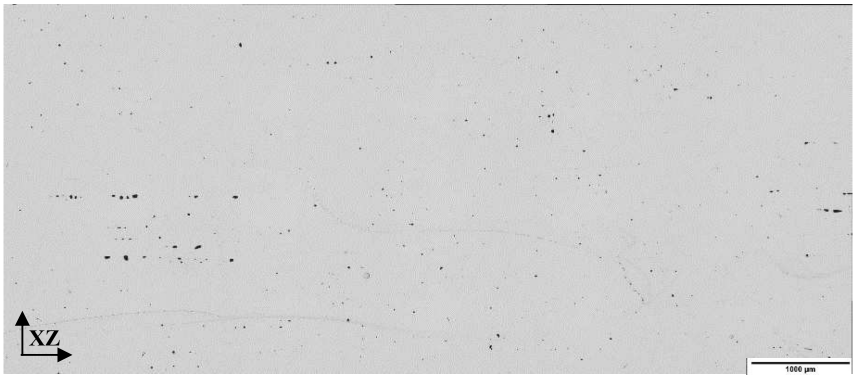

b) Case II: Low power, high dwell time, E_{as} Constan (contrast and sharpness enhanced)

Figure 3.2 As-polished stitched images for Case I and Case II in build direction for stochastic spot melt

Moreover, the metallographic etched images in the build direction for raster melt (Figure 3.3a) and stochastic spot melt (Figure 3.3b) build provide more insights into grain size for both builds.

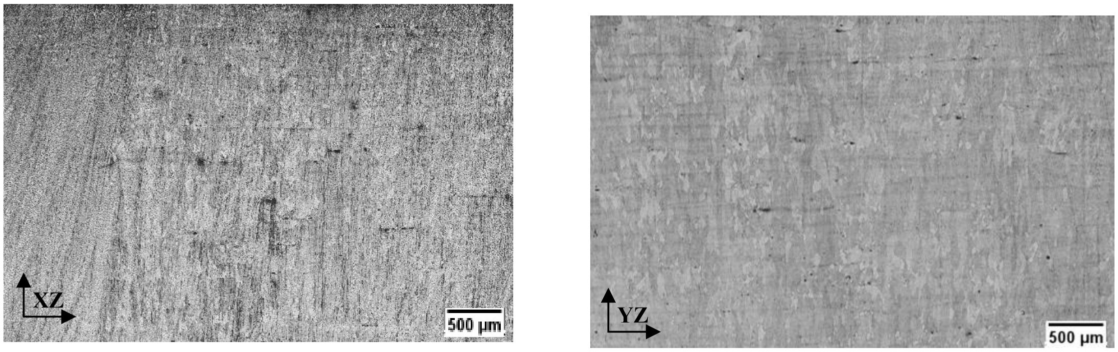

a) Raster melt microstructure in build direction (contrast and sharpness enhanced)

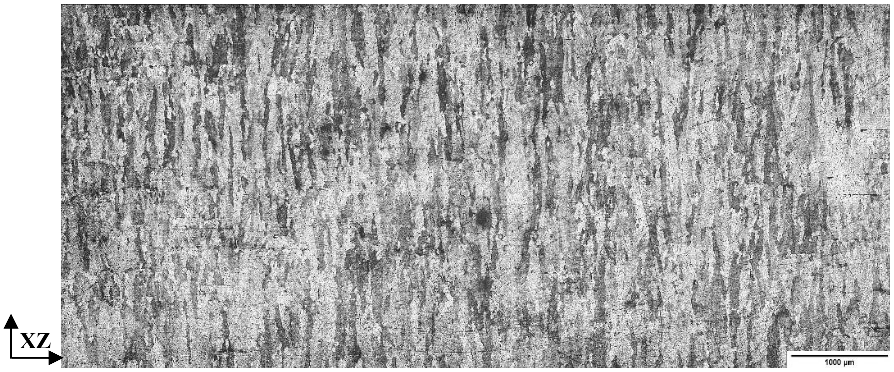

b) Stochastic spot melt microstructure (Stitched Image) in build direction (contrast and sharpness enhanced)

Figure 3.3 Etched images for Raster and Stochastic spot melting in build direction

The majority of grains appear to be columnar, accompanied by a limited presence of equiaxed grains in both the raster and stochastic spot melt build (Figure 3.3) . However, stitched images of stochastic spot melt in the build direction (Figure 3.3b) provide insights that in the edges, the grains are less columnar than the center. This could be the faster cooling rate of the edges of the specimen than the center, which yielded fewer columnar microstructures than the center.

Further insights were found in grain microstructures at the edges (Figure 3.4) for stochastic spot melt builds, when compared in case I and case II conditions as elaborated earlier. These images were taken in optical shadow mode keeping the light angle in the same direction of the etched samples. It is observed that, at near edges, even though the E_{as} was kept the same during the build, lower dwell time resulted in fewer columnar grains at the edges than the higher dwell time builds. This provides us a context that it might be possible to refine microstructures by properly altering dwell time with power in case of spot melt.

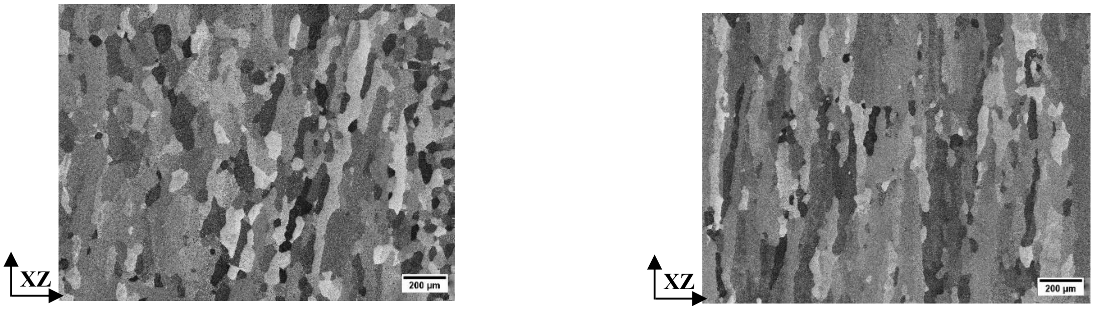

a) 540W |170µs Dwell | 9.18J/mm^2 E_{as}

b) 300W |300µs Dwell | 9J/mm^2 E_{as}

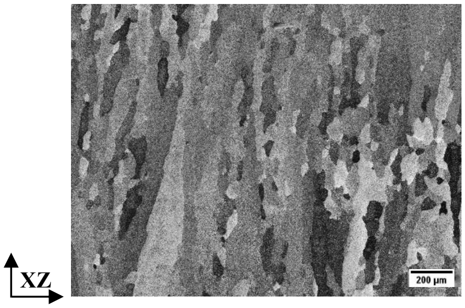

c) 360W |250µs Dwell | 9J/mm^2 E_{as}

Figure 3.4 Etched images near edges for 3 different Process parameters while maintaining similar E_{as}

Additional investigation through SEM was done to gain insights of the the grains for both strategies using backscattered (BSE) and secondary electron (SE) mode (Figure 3.5). Even though, BSE and SE mode were tweaked – not enough information for grains were found rather except the confirmation of columnar growth of grains in both cases. However, stochastic had more less visible columnar grain than raster melt.

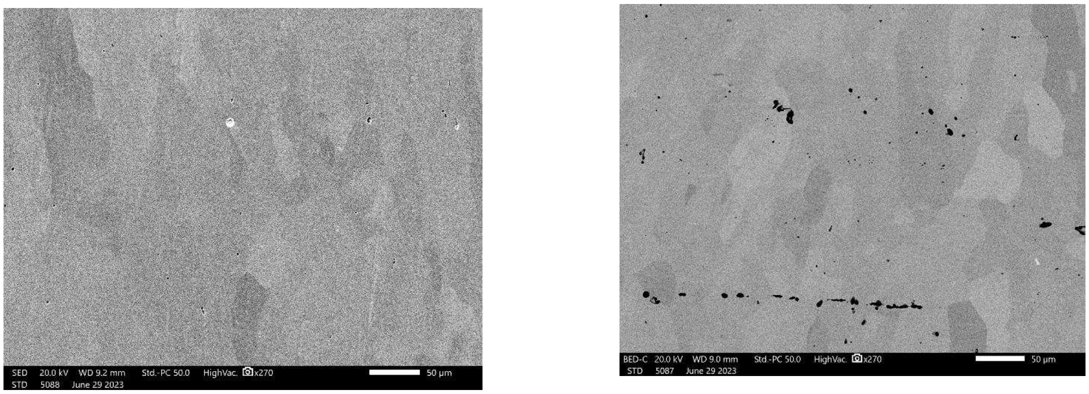

Figure 3.5 SEM images in SE and BSE Mode to evaluate microstructure
Raster (Left) ; Stochastic Spot Melt (Right) -contrast, sharpness and brightness boosted

Density and Hardness

The raster build achieved a density of 99.71% according to pycnometer measurements, and ImageJ analysis indicated a range of 99.87-99.91%. Meanwhile, for the stochastic spot melt build, the pycnometer and ImageJ results were 98.01% and 98.20%, respectively. This closer alignment may be due to the concentration of small amorphous pores, which resulted in lower density in the stochastic spot melt build.

Hardness values for the raster build and stochastic spot melt build, shown in Table 3.1. Observing Table 3.1 and the accompanying Figure 3.4, reveal that the raster build exhibits superior hardness when compared to the stochastic builds. This difference could be attributed to the internal porosity of the stochastic build, as pores can work as stress concentrators reducing hardness value.

Table 3.1 Vickers Microhardness Value (HV1) for Raster and Stochastic Builds

Build	Test 1	Test 2	Test 3	Test 4	Test 5	Mean	Overall
Raster(XZ)	433	436	417	439	433	432	431
Raster(YZ)	428	428	430	428	434	430	
Stochastic (XZ)	425	426	416	394	419	416	418
Stochastic (YZ)	403	426	419	427	422	419	

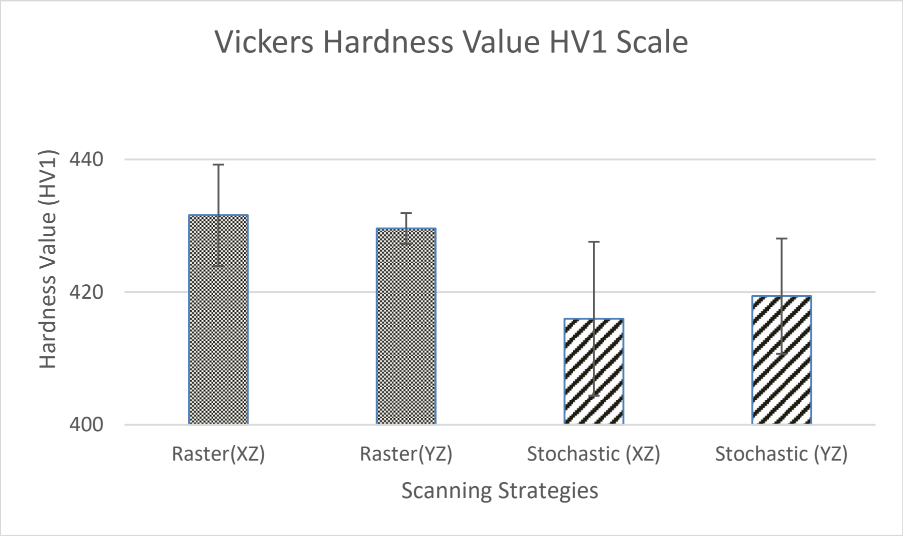

Figure 3.4 Vickers hardness value (HV1) for Raster and Stochastic builds

Overall, during builds, the raster scanning strategy, associated with a slower and more controlled melting process, yielded components with a majority of columnar grains. This is likely due to the linear beam path allowing for a more ordered melting process and more effective gas expulsion. However, for stochastic melt scanning strategy, a higher E_{as} was required during the melting process. Even though this resulted in faster melting and produced fewer columnar grains in edges when paired with higher power and lower dwell time, it resulted in regions with higher porosity in the center. This porosity might be attributed to the stochastic nature of the melting strategy. During shorter dwell time or faster melting as described in Case I (Figure 3.2a), there could a rapid localized heating that quickly forms meltpool. Since the system does not have a controlled vacuum, even in a vacuum environment this might cause certain elements in metal powders to rapidly vaporize creating a localized vapor pressure within the meltpool. This trapped vapor can affect the meltpool, leading to turbulence and forming irregularly shaped pores as the vaporized material attempts to escape (Figure 3.2a). For Case II (Figure 3.2b), longer dwell time allowed the energy spread out over longer periods. This might have allowed the meltpools to maintain a uniform temperature reducing the rapid vaporization of the metal elements. With less vapor being produced, there could be a lower turbulence in meltpool, leading to a stable melting process even though the overall energy input remained same. Further investigation needs to be evaluated to make this above statement concrete.

4 Conclusion

In summary, this study presented a comprehensive examination of the effects of raster and stochastic spot melt scanning strategies on the microstructure, density, and hardness of IN718 components produced via Electron Beam Powder Bed Fusion (EB-PBF). The distinction in terms of melt pool dynamics, thermal gradient and solidification rates arising from these strategies resulted characteristics differences in microstructural features, defect formation, and overall part performance.

A critical observation from this work is the need for careful balance of process parameters, particularly dwell time and power, to manage melting rates which affects solidification rate, prevent defects such as gas entrapped pores and keyholing, and ensure the production of high-quality parts in EB-PBF processes. Increased dwell time can alleviate the rapid melting related issues seen in stochastic spot melt, but at the risk of introducing additional energy-related defects.

These findings underscore the importance of understanding the interplay between process parameters and material properties in additive manufacturing processes like EB-PBF. They also serve to illustrate the potential of these techniques for tailoring microstructural properties to meet specific application requirements, highlighting the versatility and potential of EB-PBF in the broader field of materials engineering.

Future research should continue to explore the effect of other process parameters and further optimize scanning strategies to achieve even more precise control over the resulting microstructure and properties. This will contribute to the ongoing evolution of EB-PBF, enhancing its utility and reliability for manufacturing a diverse range of high-performance components.

Acknowledgement

The research presented here was conducted at The University of Texas at El Paso within the W.M. Keck Center for 3D Innovation (Keck Center), a 13,000-sq. ft. State-of-the-art additive manufacturing facility. The fund for this research was provided by the National Science Foundation -Grant Number 2117801. The author appreciates the assistance and opportunities extended by these institutions, which significantly contributed to the completion of this study.

References

[1] Q. C. Liu, Q. Guo, C. Li, Y. Mei, X. Zhou, and Y. Huang, "Recent progress on evaluation of precipitates in Inconel 718 superalloy," Acta Metall. Sin., pp. 1259-1266, 2016. Available: http://dx.doi.org/10.11900/0412.1961.2016.00290

[2] R. G. Ding, Z. W. Huang, H. Y. Li, I. Mitchell, G. Baxter, and P. Bowen, "Electron microscopy study of direct laser deposited IN718," Mater. Charact., vol. 106, pp. 324-337, 2015. Available: https://doi.org/10.1016/j.matchar.2015.06.012

[3] J. R. Davis, Ed., Nickel, cobalt, and their alloys, ASM International.

[4] A. Strondl, R. Fischer, G. Frommeyer, and A. Schneider, "Investigations of MX and γ′/γ″ precipitates in the nickel-based superalloy 718 produced by electron beam melting," Mater. Sci. Eng. A, vol. 480, pp. 138–147, 2008. Available: https://doi.org/10.1016/j.msea.2007.07.012

[5] D. Deng, J. Moverare, R. L. Peng, and H. Söderberg, "Microstructure and anisotropic mechanical properties of EBM manufactured Inconel 718 and effects of post heat treatments," Mater. Sci. Eng. A, vol. 693, pp. 151–163, 2017. Available: https://doi.org/10.1016/j.msea.2017.03.085

[6] P. Karimi et al., "Tailored grain morphology via a unique melting strategy in electron beam-powder bed fusion," Mater. Sci. Eng. A, vol. 824, p. 141820, Sep. 2021. Available: https://doi.org/10.1016/j.msea.2021.141820

[7] A. T. Polonsky, N. Raghavan, M. P. Echlin, M. M. Kirka, R. R. Dehoff, and T. M. Pollock, "Scan strategies in EBM-printed IN718 and the physics of bulk 3D microstructure development," Mater. Charact., vol. 190, p. 112043, Aug. 2022. Available: https://doi.org/10.1016/j.matchar.2022.112043

[8] R. R. Dehoff, M. M. Kirka, F. A. List, K. A. Unocic, and W. J. Sames, "Crystallographic texture engineering through novel melt strategies via electron beam melting: Inconel 718," Mater. Sci. Technol., vol. 31, no. 8, pp. 939–944, Oct. 2014. Available: https://doi.org/10.1179/1743284714Y.0000000697

[9] D. Deng, J. Moverare, R. L. Peng, and H. Söderberg, "Microstructure and anisotropic mechanical properties of EBM manufactured Inconel 718 and effects of post heat treatments," Mater. Sci. Eng. A, vol. 693, pp. 151–163, May 2017. Available: https://doi.org/10.1016/j.msea.2017.03.085